Interrogation of fiber Bragg-grating resonators by polarization-spectroscopy laser-frequency locking

G. Gagliardi, S. De Nicola*, P. Ferraro, P. De Natale

Consiglio Nazionale delle Ricerche-Istituto Nazionale di Ottica Applicata (INOA) and European Laboratory for Non-Linear Spectroscopy (LENS), Comprensorio "A. Olivetti", Via Campi Flegrei 34, 80078 Pozzuoli (Naples), Italy
*Consiglio Nazionale delle Ricerche-Istituto di Cibernetica "E. Caianello", Comprensorio "A. 0Olivetti", Via Campi Flegrei 34, 80078 Pozzuoli (Naples), Italy
gianluca.gagliardi@inoa.it

Abstract: We report on an optically-based technique that provides an efficient way to track static and dynamic strain by locking the frequency of a diode laser to a fiber Bragg-grating Fabry-Pérot cavity. For this purpose, a suitable optical frequency discriminator is generated exploiting the fiber natural birefringence and that resulting from the gratings inscription process. In our scheme, a polarization analyzer detects dispersive-shaped signals centered on the cavity resonances without need for additional optical elements in the resonator or any laser-modulation technique. This method prevents degradation of the resonator quality and maintains the configuration relatively simple, demonstrating static and dynamic mechanical sensing below the picostrain level.

References and links

1. B. Lissak, A. Arie, and M. Tur, "Highly sensitive dynamic strain measurements by locking lasers to fiber Bragg gratings," Opt. Lett. **23**, 1930-1932 (1998).
2. A. Arie, B. Lissak, and M. Tur, "Static Fiber-Bragg Grating strain sensing using frequency-locked lasers," J. Lightwave Technol. **17**, 1849-1855 (1999).
3. G. Gagliardi, M. Salza, P. Ferraro, P. De Natale, "Fiber Bragg-grating strain sensor interrogation using laser radio-frequency modulation," Opt. Express **13,** 2377-2384 (2005).
4. J. H. Chow, I. C. Littler, G. de Vine, D. E. McClelland, M. B. Gray, "Phase-sensitive interrogation of fiber Bragg grating resonators for sensing applications," J. Lightwave Technol. **23**, 1881-1889 (2005).
5. L. A. Ferreira, E. V. Diatzikis, J. L. Santos, and F. Farahi, "Demodulation of Fiber Bragg Grating Sensors based on dynamic tuning of a multimode Laser Diode," Appl. Opt. **38**, 4751-4759 (1999).
6. X. Wan and H. F. Taylor, "Intrinsic fiber Fabry-Perot temperature sensor with fiber Bragg grating mirrors," Opt. Lett. **27**, 1388-1390 (2002).
7. J. H. Chow, D. E. McClelland, M. B. Gray, and I. C. Littler, "Demonstration of a passive subpicostrain fiber strain sensor," Opt. Lett. **30**, 1923-1925 (2005).
8. G. Gagliardi, M. Salza, P. Ferraro, and P. De Natale, "Interrogation of FBG-based strain sensors by means of laser radio-frequency modulation techniques," J. Opt. A **8**, S507-S513 (2006).
9. F. Maystre and R. Dandliker, "Polarimetric fiber optical sensor with high sensitivity using a Fabry-Perot structure," Appl. Opt. **28**, 1995-2000 (1989).
10. R. J. Rafac, B. C. Young, J. A. Beall, W. M. Itano, D. J. Wineland, and J. C. Bergquist, "Sub-dekahertz Ultraviolet Spectroscopy of $^{199}Hg^+$," Phys. Rev. Lett. **85**, 2462-2465 (2000).
11. A. A. Abramovici, W. Althouse, R. P. Drever, Y. Gursel, S. Kawamura, F. Raab, D. Shoemaker, L. Sievers, R. Spero, K. S. Thorne, R. Vogt, R. Weiss, S. Whitcomb, and M. Zuker, "LIGO--the Laser-Interferometer-Gravitational-Wave Observatory," Science **256**, 325-333 (1992).
12. Q. A. Turchette, C. J. Hood, W. Lange, H. Mabuchi, and H. J. Kimble, "Measurement of conditional phase shifts for Quantum Logic," Phys. Rev. Lett. **75**, 4710-4713 (1995).
13. G. Hagel, M. Houssin, C. Knoop, C. Champenois, M. Vedel, and F. Vedel, "Long-term stabilization of the length of an optical reference cavity," Rev. Sci. Instrum. **76**, 123101 (2005).

14. A. Schoof, J. Grünert, S. Ritter, and A. Hemmerich, "Reducing the linewidth of a diode laser below 30 Hz by stabilization to a reference cavity with a finesse above 10^5," Opt. Lett. **26**, 1562-1564 (2001).
15. R. L. Barger, M. S. Sorem, and J. H. Hall, "Frequency stabilization of a CW dye laser," Appl. Phys. Lett. **22**, 573-577 (1973).
16. A. D. White, "Frequency stabilization of gas lasers," IEEE J. Quantum Electron. **QE-1**, 349-357 (1965).
17. T. W. Hansch and B. Couillaud, "Laser frequency stabilization by polarization spectroscopy of a reflecting reference cavity," Opt. Commun. **35**, 441-444 (1980).
18. R. W. P. Drever, J. L. Hall, F. V. Kowalski, J. Hough, G. M. Ford, A. J. Munley, and H. Ward, "Laser phase and frequency stabilization using an Optical Resonator," Appl. Phys. B **31**, 97-105 (1983).
19. M. Zhu and J. L. Hall, "Stabilization of optical phase/frequency of a laser system: application to a commercial dye laser with an external stabilizer," J. Opt. Soc. Am. B **10**, 802-816 (1993).
20. H. Stoehr, F. Mensing, J. Helmcke, and U. Sterr, "Diode laser with a 1 Hz linewidth," Opt. Lett. **31**, 736-738 (2006).
21. H. R. Telle and U. Sterr, in *Frequency Measurement and Control*, A. N. Luiten ed., (Spinger-Verlag, Berlin Heidelberg 2001).
22. M. de Angelis, G. M. Tino, P. De Natale, C. Fort, G. Modugno, M. Prevedelli, C. Zimmermann, "Tunable frequency-controlled laser source in the near ultraviolet based on doubling of a Semiconductor Diode Laser," Appl. Phys. B **62**, 333-338 (1996).
23. R. J. Forster and N. Langford, "Polarization spectroscopy applied to the frequency stabilization of rare-earth-doped fiber lasers: a numerical and experimental demonstration," J. Opt. Soc. Am. B **14**, 2083-2090 (1997).
24. N. J. Frigo, A. Dandridge, and A. B. Tveten, "Technique for elimination of polarization fading in fibre interferometers," Electron. Lett. **20**, 319-320 (1984).
25. T. Erdogan and V. Mizrahi, "Characterization of UV-induced birefringence in photosensitive Ge-doped silica optical fibers," J. Opt. Soc. Am. **11**, 2100-2105 (1994).
26. K. Dossou, S. LaRochelle, and M. Fontaine, "Numerical analysis of the contribution of the transverse asymmetry in the photo-induced index change profile to the birefringence of Optical Fiber," J. Lightwave Technol. **20**, 1463-1469 (2002).
27. G. A. Ball, G. Meltz, and W. W. Morey, "Polarimetric heterodyning Bragg-grating fiber-laser sensor," Opt. Lett. **18**, 1976-1978 (1993).
28. B. J. Eggleton and R. E. Slusher, in *Nonlinear Photonic Crystals*, B. J. Eggleton and R. E. Slusher eds., (Spinger-Verlag, Berlin Heidelberg 2003).
29. S. T. Oh, W. Han, U. Paek, and Y. Chung, "Discrimination of temperature and strain with a single FBG based on the birefringence effect," Opt. Express **12**, 724-729 (2004).
30. J. E. Sipe, L.Poladian, and C. Martijn de Sterke, "Propagation through nonuniform grating structures," J. Opt. Soc. Am. A **11**, 1307-1320 (1994).
31. Corning, "SMF-28 Product Information Sheet," (One Riverfront Plaza, Corning, N.Y. 14831, 2001).
32. J. H. Chow, B. S. Sheard, D. E. McClelland, M. B. Gray, and I. C. M. Littler, "Photothermal effects in passive fiber Bragg grating resonators," Opt. Lett. **30**, 708-710 (2005).
33. I. C. M. Littler , T. Grujic, and B. J. Eggleton, "Photothermal effects in fiber Bragg gratings," Appl. Opt., **45**, 4679-4685 (2006).
34. A. D. Kersey, T. A. Berkoff, and W. W. Morey, "Fiber-optic Bragg grating strain sensor with drift-compensated high-resolution interferometric wavelength-shift detection," Opt. Lett. **18**, 72-74 (1993).

1. Introduction

Interrogation of fiber Bragg-grating (FBG) structures by laser spectroscopic techniques has proved in recent years to be very promising for development of highly-sensitive mechanical sensors. In most cases, a strong sensitivity enhancement in detection of dynamic strain has been obtained relying on laser-frequency modulation techniques that are capable to extract from the FBG-reflected light wavelength-encoded information on the measurand [1-5]. Particularly, the use of high-finesse fiber-Bragg-grating Fabry-Pérot (FBGFP) cavities as thermo-mechanical gauges has been demonstrated in a laser-to-cavity lock fashion, achieving a high sensitivity in detecting temperature changes [6], dynamic strain [7, 8] and pressure [9]. On the other hand, high-precision and high-sensitivity spectroscopy as well as gravitational waves and cavity quantum electrodynamics experiments have strongly relied on precise stabilization of laser frequency to external optical resonators [10-14]. Over the last decades, several different methods have been implemented for this purpose, including side-of-fringe locking [15], transmission derivative spectroscopy [16], reflection polarization spectroscopy [17], and the most popular Pound-Drever-Hall (PDH) sideband technique [18-20]. In the work by Chow et al. [7], two different PDH locks were devised, one for dynamic interrogation of a

passive FBG-resonator, and another to reduce intrinsic laser-frequency jitter prior to locking the laser to the strain-sensing fiber cavity. Polarization spectroscopy method would be very attractive in this respect, since no modulation technique is necessary to obtain laser stabilization. If a linear polarizer is placed inside the cavity, the reflected light acquires a frequency-dependent elliptical polarization that is detected by a polarization analyzer generating dispersion-shaped resonances. This provides an ideal error signal for frequency correction, being steep around the resonance with far-reaching wings [17]. So far, the main drawback for most applications has been the need for a polarizing element between the mirrors, which significantly degrades the cavity finesse, thus limiting its applicability [21, 22]. In a limited number of optical fiber-based systems, a similar polarization-sensitive scheme has been successfully applied mostly to prevent laser-cavity mode-hopping and polarization-induced fading in interferometers, using weakly-birefringent fibers [23, 24].

In this paper, we propose a different way to interrogate a single-mode FBGFP sensor, extending the polarization-spectroscopy scheme by Hansch et al. [17] to lock a diode laser to the fiber resonator. Our method is based on polarization analysis of the reflected radiation without any internal polarizer. We theoretically investigate and experimentally demonstrate that the anisotropy induced into the FBG during the inscription process [25-29], combined to the natural birefringence of the pristine fiber, gives rise to the same ellipticity effect as by a polarizer placed into the cavity. Finally, we show examples of the FBGFP operation as a static and dynamic strain sensor using the intracavity fiber as a sensitive element.

2. Theoretical model

Let us first study the polarization-dependent complex response of a resonator made of two coupled, highly-reflective FBGs. We consider two uniform, not apodized, Bragg gratings of length L, spaced by a distance L_d along the z axis of a single-mode (SM) optical fiber. As a consequence of the inscription process, a local anisotropy may be produced in the grating fiber. We thus assume that the two FBGs are both affected by a certain amount of birefringence along their physical length L so that the refractive-index modulations δn_x and δn_y and background refractive-index variations σ_x and σ_y along two transverse orthogonal directions x and y of the FBGFP frame are different and the cavity has two, possibly non-degenerate orthogonal polarization eigenmodes corresponding to two different grating structures along the $i = (x, y)$ direction. Accordingly, we model the indexes of refraction of our birefringent grating as $n_i(z)/n_{b,i} = 1 + \sigma_i + \delta n_i \cos(2\pi z/p)$, where $n_{b,i}$ are the mean refractive indexes of the structure, related to the corresponding Bragg wavelengths $\lambda_{b,i}$ by $\lambda_{b,i} = 2p n_{b,i}$, where p is the modulation period of both gratings. We also assume positive grating amplitudes $\kappa_i = \delta n_x / 2 n_{b,i} \ll 1$ and background refractive-index variations $|\sigma_i| \ll 1$.

In order to analyze this structure we apply the effective-medium approach (EMA) to find the transmission and reflection coefficients along the i-direction of the FBGFP [30]. According to EMA, we may immediately write down the reflection and transmission coefficients ρ_i and τ_i of a uniform grating of length L surrounded by a region with no grating

$$\rho_i = \frac{r_{12,i}\left[1 - \exp\left(-2jkn_{eff,i}L\right)\right]}{1 - r_{12,i}^2 \exp\left(-2jkn_{eff,i}L\right)} \tag{1a}$$

$$\tau_i = \frac{\left(1 - r_{12,i}^2\right)\exp\left(-2jkn_{eff,i}L\right)}{1 - r_{12,i}^2 \exp\left(-2jkn_{eff,i}L\right)} . \tag{1b}$$

In Eq. (1a-1b) we have $j = \sqrt{-1}$ and the effective refractive index $n_{eff,i}$ for the i-direction given by

$$n_{eff,i} = \sqrt{(\Delta_i + \sigma_i)^2 - \kappa_i^2} \quad , \tag{2a}$$

where $\Delta_i = (k_i - k_{b,i})/k_{b,i}$ is the detuning parameter of the wave number $k_i = 2\pi n_{b,i}/\lambda$ with respect to the nominal resonance wave number $k_{b,i} = 2\pi n_{b,i}/\lambda_{b,i}$ at the Bragg wavelength $\lambda_{b,i}$ and $r_{12,i}$ is the reflection coefficient at the interface between the i-grating and the surrounding medium, namely $r_{12,i} = (Z_i - 1)/(Z_i + 1)$ where the effective impedance Z_i is given by

$$Z_i = \left(\frac{\Delta_i + \sigma_i - \kappa_i}{\Delta_i + \sigma_i + \kappa_i} \right)^{1/2} \quad . \tag{2b}$$

EMA provides a convenient way to calculate the reflection coefficient R_i of the i-cavity. In fact, in the framework of the EMA, the whole cavity can be treated as a multilayered structure, composed by a sequence of three media, a first grating of length L with reflection and transmission coefficients ρ_i and τ_i (cfr. Eq. 1a-1b), followed by a region of length L_d with no grating and a second grating, identical to the first one. Proceeding as in the standard optics of multilayer films we multiply the corresponding optical matrices and easily obtain the cavity reflection coefficient

$$R_i = \frac{\rho_{,i}[1 + \exp[-j(\chi_i + 2k\,n_{eff,i}L_d)]]}{1 - \rho_i^2 \exp(-j2k n_{eff,i}L_d)} \quad , \tag{3}$$

where we have defined the phase χ_i in the following form

$$\chi_i = \arctan\left(\frac{1 + r_{12,i}^2}{1 - r_{12,i}^2} \tan(k n_{eff,i}L) \right) \quad . \tag{3a}$$

A polarimetric characterization of the cavity can be done using a simple experimental arrangement. Resonant laser radiation is adjusted to a variable linear polarization state by a rotator and the state of polarization (SOP) of the reflected beam is analyzed through a sequence of a quarter-waveplate ($\lambda/4$) and a polarizing beam-splitter (PBS). For a linear input field $E_{inc} = [E_{inc,\perp}\ E_{inc,\|}]^T$, where $E_{inc,\perp}$ and $E_{inc,\|}$ are the electric field amplitudes perpendicular and parallel to the PBS axes (laboratory frame axes), respectively, the corresponding reflected intensities, $I_{R,\perp}(\lambda)$ and $I_{R,\|}(\lambda)$, after the $\lambda/4$-PBS system, are given by

$$I_{R,\perp}(\lambda) = \left| P_\perp \Re(\lambda/4)\Re(-\theta)R(\lambda)\Re(\theta)E_{inc} \right|^2 \tag{4a}$$

$$I_{R,\|}(\lambda) = \left| P_\| \Re(\lambda/4)\Re(-\theta)R(\lambda)\Re(\theta)E_{inc} \right|^2 , \tag{4b}$$

where the Jones matrices $P_\perp = [(1,0)(0,0)]$, $P_{\|} = [(0,0)(0,1)]$ select the polarization along the two PBS axes, respectively, $\Re(\lambda/4)$ is the matrix of the quarter-wave plate ($\lambda/4$), $R = [(R_x,0)(0,R_y)]$ the reflection matrix of the FBGFP structure in terms of the reflection

coefficients R_x and R_y, given by Eq. (3a) and Eq. (3b), and $\Re(\theta)$ the rotation matrix of angle θ, which accounts for possible misalignment of the FBGFP axes with respect to the laboratory frame axes. For a linear input SOP at an angle α in this frame (i.e. the PBS's), the corresponding reflected intensities $I_{R,\perp}(\lambda)$ and, $I_{R,\parallel}(\lambda)$ determined by Eq. (4a-4b), can be written as

$$I_{R,\perp} = \frac{1}{2}\left|R_x \cos(\alpha-\theta) - j\sin(\alpha-\theta)R_y\right|^2 \tag{5a}$$

$$I_{R,\parallel} = \frac{1}{2}\left|R_y \sin(\alpha-\theta) - j\cos(\alpha-\theta)R_x\right|^2 , \tag{5b}$$

when the $\lambda/4$ axis is set at 45°. Eq. (5a) and Eq. (5b) clearly show that the spectral response of the reflected intensities depends on the angle mismatch $\delta = \alpha - \theta$ between the linear input SOP and the FBGFP axes.
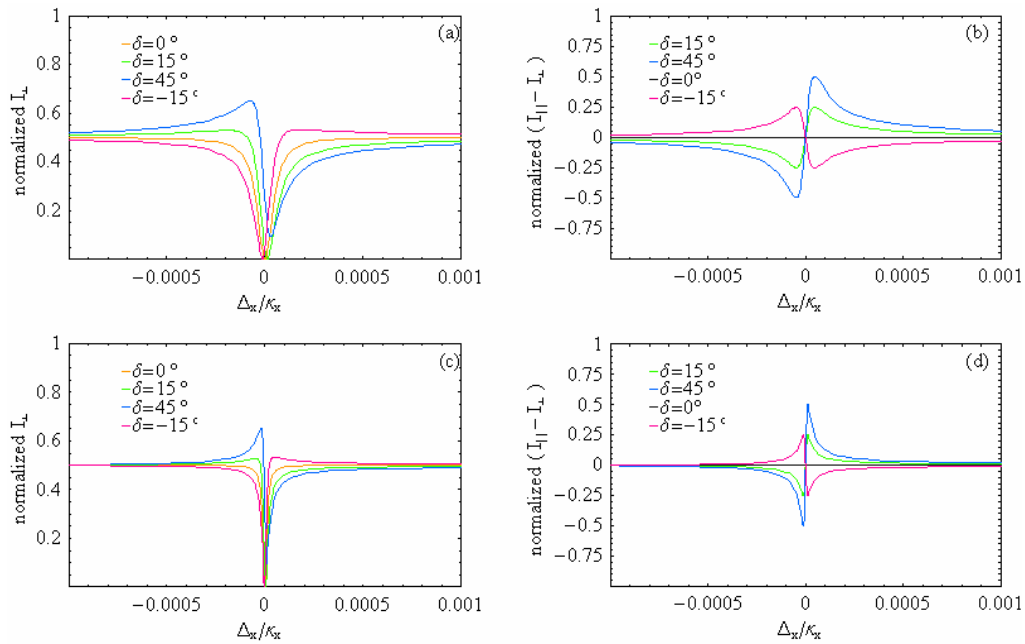

Fig. 1. (a). Numerical response of the reflected signal $I_{R,\perp}$ vs. the normalized detuning ratio for different mismatch angles δ ($\lambda/4$ set at 45°; $n_{b,x}=1.468$ $\delta n_x = \delta n_y = 1.7\times10^{-4}$; $\sigma_x = \sigma_y = 0$; $\Delta n = n_{b,y} - n_{b,x} = 1\times10^{-6}$ for silica). b) The simulation is repeated for the difference of polarization components $I_{R,\parallel} - I_{R,\perp}$. In c) and d) $I_{R,\perp}$ and the difference $I_{R,\parallel} - I_{R,\perp}$, respectively, are calculated for $\delta n_x = \delta n_y = 2\times10^{-4}$ with the same parameters as in a).

From Eq. (5a) – Eq. (5b) we can also derive an expression for the difference of the intensities in terms of the complex reflection coefficients, namely

$$I_{R,\parallel} - I_{R,\perp} = \frac{1}{2}\sin(2(\alpha-\theta))\left(R_x^* R_y - R_x R_y^*\right) . \tag{6}$$

The numerical example shown in Fig. 1(a) illustrates the typical spectral response of the reflected signal $I_{R,\perp}$ plotted as function of the detuning ratio normalized to the grating modulation $\Delta_x/\kappa_x = (k_x - k_{b,x})/k_{b,x} \kappa_x$, for different values of the angle mismatch δ, with the axis of $\lambda/4$ plate set at 45°.
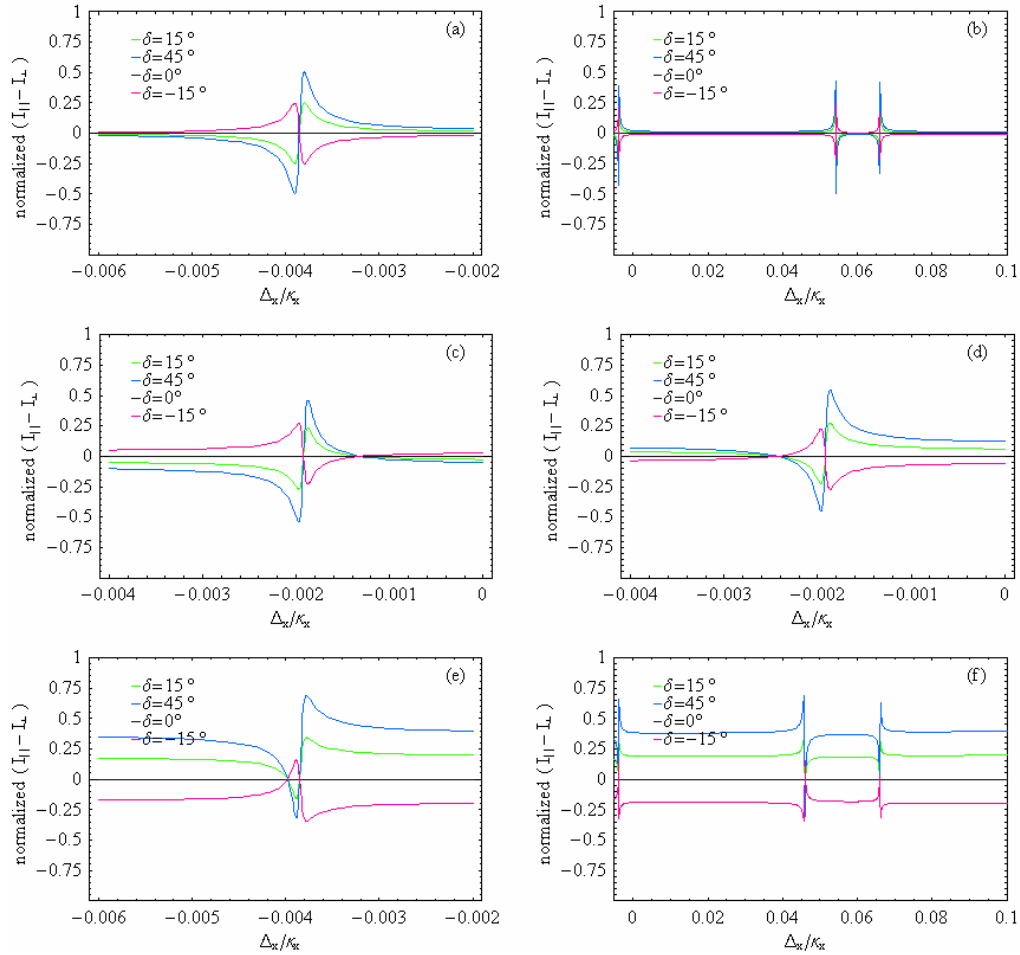

Fig. 2. The difference of PBS signals is evaluated for different grating-inscription induced birefringence: (a) the background refractive index variations are equal, $\sigma_x = \sigma_y = 1 \times 10^{-5}$ and the profiles are symmetric like in Fig. 1(b); b) here the situation (a) is shown in an extended spectral window where orthogonally-polarized eigenmodes can be both observed within a FSR; c) $I_{R,\parallel} - I_{R,\perp}$ calculated for $\sigma_x = 0.5 \times 10^{-5}$ and $\sigma_y = 0$.; d) $\sigma_x = 0$ and $\sigma_y = 0.5 \times 10^{-5}$; e) the difference signals is plotted for $\sigma_x = 1 \times 10^{-5}$ and $\sigma_y = 3 \times 10^{-5}$; f) the previous case is represented in an extended window.

Two matched 99.5-% reflectivity Bragg gratings, centered around 1560 nm, each 10-mm long and spaced by 130 mm, have been considered with $n_{b,x} = 1.468$, equal grating modulation $\delta n_x = \delta n_y = 1.7 \times 10^{-4}$ and background index variations $\sigma_x = \sigma_y = 0$. We have assumed a

natural birefringence from silica $\Delta n = n_{b,y} - n_{b,x} = 1 \times 10^{-6}$ (very close to the upper limit for individual SMF-28 fibers [31]) with axes parallel to the FBG's. Actually a possible angular mismatch between the silica and FBG birefringence axes could be taken into account by including additional rotation matrices in Eq. (4a) and Eq. (4b). However, the introduction of such angular mismatch only complicates the analysis without substantially changing the results as it can be included in the initial angle δ between the input state and the FBG.

The deep minimum in the spectral response at the resonance is obtained when $\delta = 0$, i.e., in our case, when the input polarization is aligned along the FBG's x-axis. Increasing the angle mismatch, the reflected intensity evolves into a dispersion-shaped curve vs. wavelength. Close to the resonance, the spectral behavior shown in Fig. 1(a) is to a good approximation linear, with slope increasing for larger δ angles. The slope is maximum for $\delta = 45°$. Figure 1(b) displays the spectral dependence of the difference $I_{R,\parallel} - I_{R,\perp}$. The curve symmetrically crosses zero at the resonance irrespective of the angle mismatch, thus providing and ideal frequency discriminator for servo-locking the laser.

Even larger values of the grating amplitude can be obtained when fabricating fiber gratings by UV-inscription, particularly when a high-reflectivity is produced with deep index modulation [25, 26]. Figure 1(c) and Fig. 1(d) show the spectral dependence of $I_{R,\perp}$ and of the corresponding difference $I_{R,\parallel} - I_{R,\perp}$ calculated for $\delta n_x = \delta n_y = 2 \times 10^{-4}$ and for the same parameters as in Figs. 1(a)-1(b). Increasing the value of the grating modulation shrinks the dispersion-shaped signal since the resonance becomes sharper but the slope of the dispersion-shaped signal around the resonance is still maximized for $\delta = 45°$, like in the case of a free-space resonator [17].

Figure 2 shows the effect on the dispersion shaped profile of background refractive-index variations σ_x and σ_y, possibly due to the gratings fabrication. In Fig. 2(c), the numerical calculation of difference $I_{R,\parallel} - I_{R,\perp}$ is represented for $\sigma_x = 0.5 \times 10^{-5}$ and $\sigma_y = 0$ and the same parameters as in Fig 1(b). The curve is shifted to a small negative detuning value while the average amplitude level is no longer equal to zero and changes according to the angular mismatch δ with a maximum variation at $\delta = 45°$; in Fig. 2(a) the background refractive index variations are equal, $\sigma_x = \sigma_y = 1 \times 10^{-5}$ (thus without causing any effective birefringence) and the dispersion shaped signals for different δ are again symmetric around the zero level like in Fig. 1. In Fig. 2(d), $\sigma_x = 0$ and $\sigma_y = 0.5 \times 10^{-5}$: in this case, the absolute value $|\sigma_y - \sigma_x| = 0.5 \times 10^{-5}$ is the same as in Fig. 2(c) and the offset levels for different δ are inverted with respect to zero. In Fig. 2(e), we have calculated the dispersion-shaped signals for $\sigma_x = 1 \times 10^{-5}$ and $\sigma_y = 3 \times 10^{-5}$. In addition, Fig. 2(b) and Fig. 2(f) show cases a and e, respectively, in an extended window comprising a whole free spectral range, i.e. a detuning $p/\kappa_x L_d$.

It is interesting to note that when the inscription-induced effect, considered through $\sigma_{x,y}$ grating parameters, is present with a non-zero birefringence, the symmetric lineshape for the differential cavity reflection is no longer obtained for a 45° polarization angle [see Fig. 2(e) and 2(f)]. That can be accomplished by a slight correction on the input polarization state, restoring the symmetry and the zero-crossing condition at the center.

As can be deduced from numerical results, the natural fiber birefringence contribution cannot be discriminated from the inscription-induced effect, which must be taken into account for a correct polarization analysis of the cavity reflection response.

3. Experimental approach and results

The experimental arrangement used for the polarization-spectroscopy interrogation technique is schematically shown in Fig. 3. An extended-cavity diode laser (Toptica DL-100), emitting around $\lambda = 1560$ nm with a linewidth < 500 kHz and a maximum power of 5 mW, is adopted as a coherent radiation source. The diode is temperature-controlled by a Peltier-based stabilizer and is driven by a low-noise current supply from a minimum current of 55 mA to a maximum of 200 mA. Laser radiation passes through a Faraday optical isolator and is then coupled to a single-mode polarization-maintaining (PM) fiber, where a pig-tailed linear polarizer (P) sets its initial SOP. All the remaining parts are made of conventional single-mode silica fibers. The beam is polarization controlled by a fiber-coupled half-wave plate ($\lambda/2$) and subsequently injected into the FBGFP resonator via an optical circulator to observe its transmission and reflection fields. All fibers are kept well fixed along the beam path while angled connectors and index-matching gel are used to minimize spurious reflections.
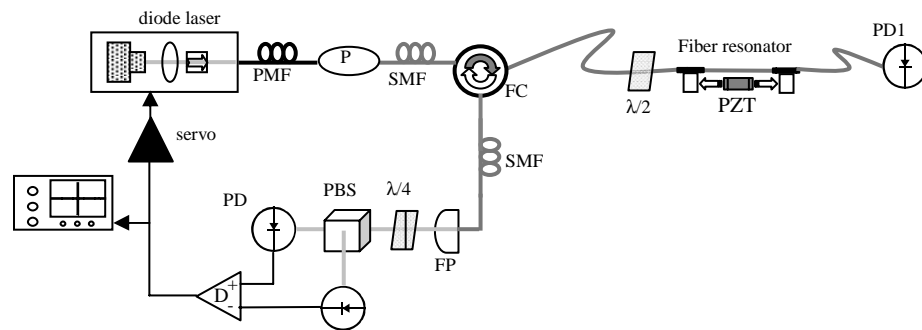

Fig. 3. Experimental set-up. P: polarizer; FC: fiber circulator; PBS: polarizing cube beamsplitter; PZT: piezo-electric transducer; PD: photodiode; D: differential amplifier; FP: fiber port; SMF: single-mode fiber; PMF: polarization-maintaining fiber.

The optical cavity reflectors are two identical single-mode fiber Bragg-gratings, with nominal reflectivity of 99.9 % (finesse $\cong$ 3000) at 1560.6$\pm$ 0.1 nm, fabricated in a single phase-mask writing process, in the same fiber, with a center-to-center distance of about 130 mm. The absence of spliced internal connections limits extra losses in the cavity and, at the same time, ensures that any anisotropy induced by the inscription process and its direction in space are likely the same for both gratings. Actually, the overall quality factor of the cavity can be strongly affected by UV-induced in-fiber losses and to a lesser extent by Bragg mirrors spectral overlap (linewidth $\approx$ 0.6 nm), as their reflectivities might not be perfectly identical. From an estimate of the cavity linewidth, we inferred an effective finesse factor F of approximately 250 for the FBGFP. From this value, given a grating nominal transmittivity T, we calculated an additional single-pass loss $\alpha \approx (\pi/F)\text{-}T \approx 0.01$, which is compatible with previous reported values [32, 33]. The FSR was measured to be 759.6 $\pm$ 0.1 MHz, which is close to the theoretical value. The FBGs are enclosed in metallic cylinders in order to keep them insensitive to mechanical deformations, making the actual free-fiber distance between the cylinders shorter than 130 mm. The cylinders are then separated by 75 mm (intracavity length) and fixed by two metallic mounts, exerting only a weak tension to the fiber without torsion. A piezo-electric transducer (PZT) is placed between them to apply length modulation. The FBGFP is closed into a thermally-insulated box in order to keep the refractive index of the intra-cavity fiber reasonably stable during the measurement time, while the laser is protected by a damping enclosure to partially prevent acoustic pollution. The whole

interrogation system is placed on a 450–mm thick optical table equipped with self-leveling pneumatic isolation.

The SOP of the incident beam can be changed in a controlled manner thanks to the fiber-coupled half-wave plate ($\lambda/2$) placed just before the cavity. The FBGFP transmitted power is monitored by a pig-tailed InGaAs PIN photodetector. The field reflected from the circulator is analyzed by a quarter-wave plate and a polarizing beam-splitter (PBS), which separates orthogonal components, and detected by two 50-MHz-bandwidth pre-amplified InGaAs photodiodes. As a first test, the diode laser was swept over a cavity mode (at a frequency of about 100 Hz) and, from the cavity-reflected optical power, the difference between the PBS transmission and reflection was observed. The spectra recorded after a 1-MHz differential amplifier (D) are shown in Fig. 4 for different mismatch angles, starting from the SOP that minimizes the transmission of one cavity eigenmode (0°). The response is in qualitative agreement with the numerical simulations although the periodic behavior of dispersive profiles has a different dependence on the angle δ. Small differences between the real birefringence value and that assumed in the model may play a relevant role in this respect.
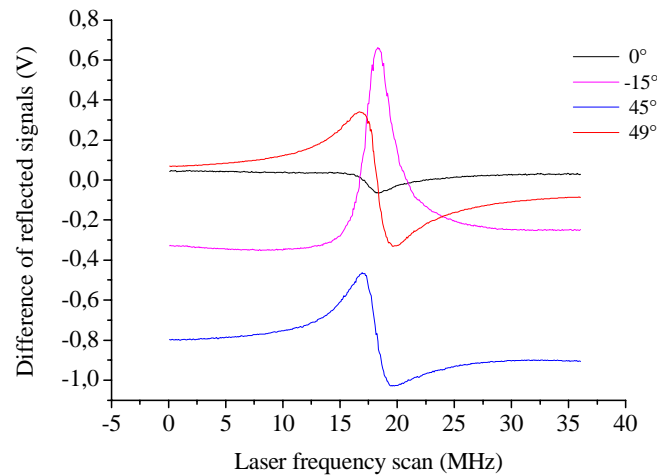

Fig. 4. Laser scan showing the differential reflection lineshape of one single cavity eigenmode, at variable input angles, detected after the PBS analyzer and the amplifier D.

According to manufacturer's data, the polarization-mode dispersion (PMD) of the internal single-mode fiber corresponds to a Δn variation ranging from 10^{-7} to 10^{-6}, like for most silica fibers [31]. This suggests that the polarization-sensitive response can be ascribed both to the gratings and to the fiber itself, as assumed in the simulation above. Slight profile asymmetries may be also present due to the laser-current scan as well as the photothermal effect [32, 33] caused by fiber losses during the resonator build-up. The signal with the maximum slope and symmetry around the Airy resonance is experimentally obtained for a $\lambda/2$ rotation of about 48° (red trace in Fig. 4) with respect to the initial SOP (red trace in Fig. 4).
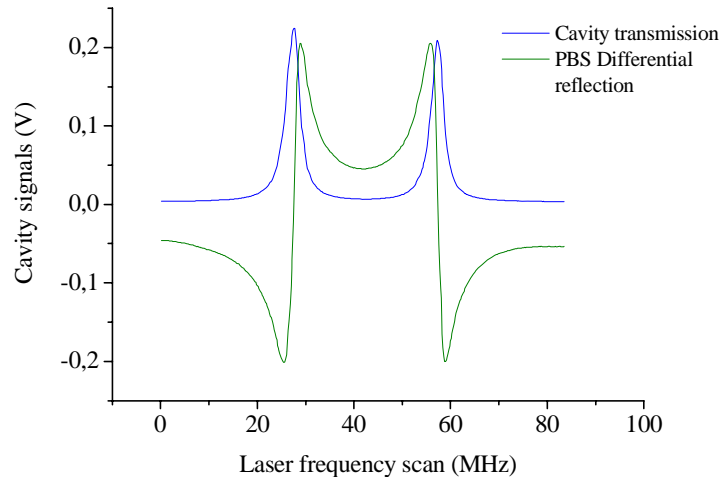
Fig. 5. Transmission (blue trace) and differential reflection (green) simultaneously detected for fast and slow cavity eigenmodes.

In this condition, the difference between the PBS components, obtained from the amplifier D, is symmetrical and crosses zero exactly at the center, the quarter-wave plate (λ/4) enabling for a fine balance of the two beams at the detectors. It is important to point out that the optimal angle can be determined experimentally without a-priori knowledge of the FBGFP axes in the PBS frame. Indeed, the actual orientation with respect to the laser incident SOP can be found by rotating the λ/2 and observing the cavity eigenmodes on the transmission. Similar profiles can be observed for both polarization states in coincidence with a transmission peak, which confirms that a polarization ellipticity upon reflection is definitely due to the cavity. In Fig. 5, the transmission and polarization-selected reflection signals for fast and slow axes of the fiber have been recorded along the same laser scan, when the input polarization is adjusted to excite both orthogonally-polarized modes with almost the same efficiency. The two differential-reflection curves have their zero-crossing points centered exactly at the transmission peaks, with linear slopes ~ 190 nV/Hz, and opposite values as predicted by the theoretical model [see Fig. 2(f)]. We did not observe significant changes in the overall behavior when exchanging the input with the output FBG, which indicates that possible small differences between their intrinsic birefringence and axes orientation do not seriously affect the method.

The D output serves as an error signal of a home-made, integrating servo circuit that corrects laser frequency fluctuations relative to the cavity and thus enables for active laser-locking on a resonance. The servo output, i.e. the correction signal, is fed back to the laser to obtain frequency stabilization. In particular, the servo circuit is designed to direct its frequency correction simultaneously to the laser extended-cavity PZT and the current, within a maximum electronic bandwidth of the order of 1 kHz and 200 kHz, respectively. The low and high-frequency stages can be controlled independently. In Fig. 6(a), the loop action during a laser sweep over a cavity longitudinal mode is shown when the laser is being locked on the corresponding peak. The cavity transmission and the error signal from the differential amplifier clearly exhibit the effect of increasing closed-loop gain compared to the free-running condition: the intensity tends to a maximum while the error starts decreasing. Accidental locking to the adjacent "orthogonal" mode cannot occur as the two error signals are naturally in anti-phase (Fig. 5). The closed-loop FFT spectrum is also shown in Fig. 6(b), evidencing a frequency-noise reduction of a factor higher than 200 from DC to 2 kHz, when the servo gain and bandwidth are optimized.
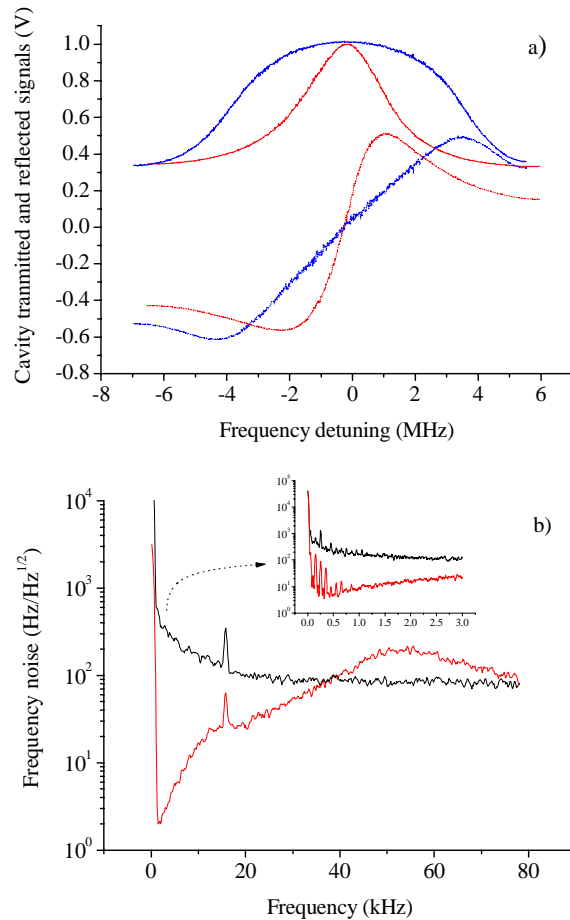
Fig. 6. Example of laser frequency stabilization for interrogation of the fiber cavity. (a). Feedback action on the cavity transmission (upper curves) and differential reflection (lower curves) for a weak closed-loop gain (blue lines) and a free-running laser (red lines) while the frequency is being scanned. (b). The maximum frequency-noise suppression can be appreciated from FFT spectrum of the error signal in the tightly-locked operation (red) with respect to the unlocked case (black), with a 500-Hz resolution (averaged over several acquisitions). The sharp peak around 16 kHz is apparently due to electrical pick-up. An auto-oscillation with significant noise increase occurs above 40 kHz, setting the upper limit of the lock bandwidth. The inset shows a detail of the frequency-noise spectrum on a kHz scale (10-Hz resolution).

A sharp peak appears around 16 kHz and is present even in absence of radiation, probably due to electronic pick-up. The whole lock unity-gain point occurs approximately at 40 kHz. Above this frequency, the response is limited by auto-oscillations due to combination of the servo circuitry with the current-driver summing stage, as visible in the spectrum. In the inset, the servo action is also shown on a much-lower frequency scale where the laser PZT works at its best. The locking ensemble exhibits remarkable time stability. Indeed, we tested the system while under use and verified that it remains locked for a period of at least 1 hour, despite possible small birefringence fluctuations in the fiber set-up.

With this in mind, the closed-loop correction signal sent to the laser acts as a monitor of the strain, $\varepsilon = \delta L_d / L_d$, suffered by the intra-cavity fiber within the servo electronic bandwidth. In Fig. 7, the FFT spectrum with excitation of a dynamic strain into the cavity fiber is shown on an acoustic frequency scale. The sharp peak at 1.24-kHz is due to a sine voltage applied to the PZT with a rms amplitude corresponding to 0.7 nε, which is used for conversion of the

vertical axis into equivalent strain-noise spectral density units ($\varepsilon_{rms}/\sqrt{Hz}$), taking into account a 10-Hz resolution bandwidth.
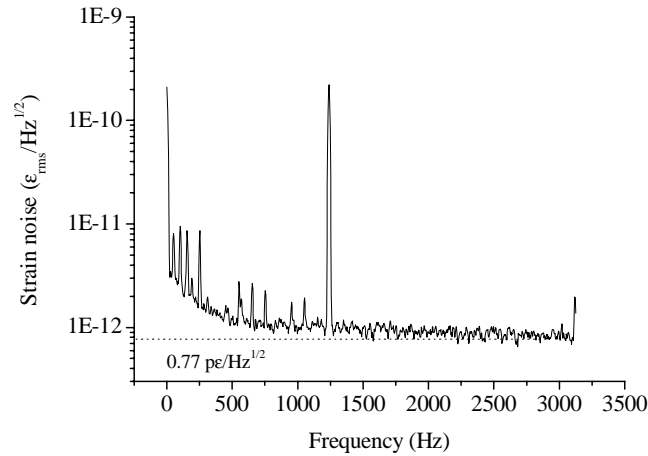

Fig. 7. Detection of dynamic strain in the FBG cavity. The plot corresponds to the FFT of the correction signal in the acoustic range for a 0.7-nε rms deformation at 1.24 kHz (20-spectra average). The dotted line at 0.77 p$\varepsilon/\sqrt{Hz}$ represents the noise floor.

A calibration of the actual displacement along the free fiber in terms of the PZT-signal has been preliminarily carried out, as a function of frequency, measuring the corresponding cavity-length modulation, with laser RF sidebands as precise frequency markers on the cavity transmission. In this way, we have taken into account the PZT effective response and mechanical coupling to the metallic mount that holds the fiber.

From Fig. 7, a noise-limited strain sensitivity as low as 0.77 p$\varepsilon/\sqrt{Hz}$ rms can be extracted by a signal-to-noise ratio of nearly 50 dB. A number of satellite oscillations are visible in the spectrum within 1 kHz, which can be attributed to acoustic resonances of the fiber, the resonator being not completely shielded against external noise. For our set-up, taking into account a signal reflected by the FBGFP of nearly 1.7 V and a detector transimpedance gain of 10^4, the shot-noise limited minimum detectable strain [2] would correspond to about 12 Hz/$\sqrt{Hz}$ $\times$ $\lambda/(0.79c) \cong$ 80 f$\varepsilon/\sqrt{Hz}$ rms (λ is 1560.5 nm, c is the speed of light in vacuum). Nevertheless, this is not a realistic estimate since many other noise sources usually dominate over the shot noise. Indeed, major limitations for dynamic measurements come from residual laser-frequency jitter relative to the cavity and thermally-induced refractive-index fluctuations [2] that contribute to the noise floor. From the free-running laser frequency-noise spectral density around 1 kHz, visible in the inset of Fig. 6(b), a frequency jitter relative to the cavity of 127 Hz/$\sqrt{Hz}$ can be observed. Hence, by direct frequency-to-strain noise conversion, one would expect the ultimate resolution to be roughly 0.8 p$\varepsilon/\sqrt{Hz}$ that is consistent with the experimental findings. Similarly, the FFT spectrum of the correction signal for a strain excitation at 2.44-Hz is shown in Fig. 8(a), yielding a minimum detectable level of 42 p$\varepsilon/\sqrt{Hz}$ rms. At low Fourier frequencies the sensitivity degrades, as expected from the net frequency-noise increase visible in Fig. 6(b). In this range, ambient noise stimulations become dominant while possible etalon effects along the optical path and polarization instability due to ambient perturbation may add noise to the error signal and thus affect the sensitivity. In Fig. 8(b), the time-domain correction signal is also represented on a 15-s scale to track 12-nε quasi-static loads on the intra-cavity fiber, caused by subsequent voltage steps on the PZT. Since the laser tunability is dictated by the mode-hop-free PZT tuning interval (~10 GHz), in principle the servo-limited dynamic range of our system can be as high as 70 $\mu\varepsilon$ from DC to 40 kHz, in locked operation. Therefore using the in-loop correction signal enables for simultaneous

quasi-static and dynamic strain detection, below the unity-gain point of the cavity lock, and significantly extends the measurement dynamics. For detection of faster strain signals, above the servo unity-gain point, the polarization-detected error signal can be directly used with consequent reduction of the sensor range.
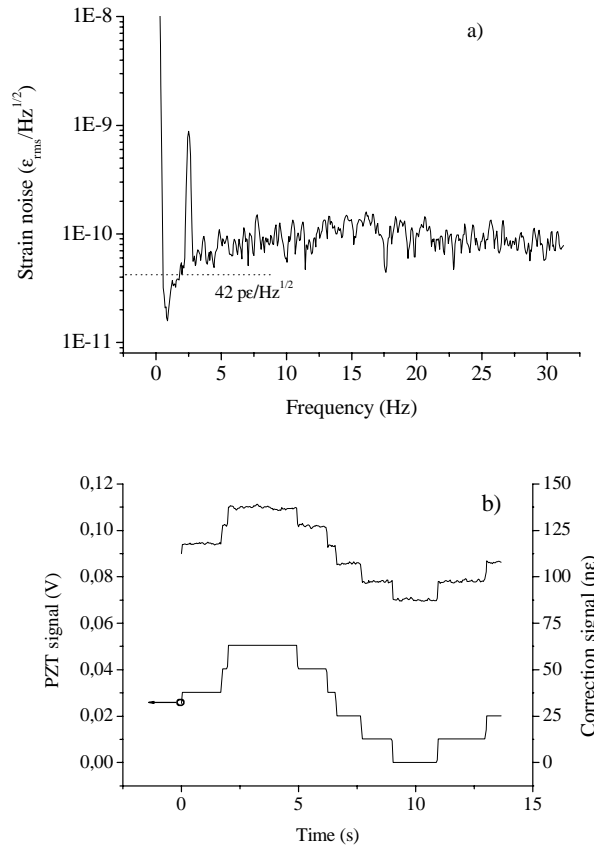

Fig. 8. (a). The response for a low frequency signal (2.44 Hz) is shown for a rms amplitude of 0.4 nε. The dotted line corresponds to a strain-equivalent noise-limited sensitivity of 42 pε/√Hz (5-spectra average). (b). Detection of quasi-static strain in the FBG cavity vs. time (15 s), for 12-nε steps applied to the fiber via the PZT.

The polarization-spectroscopy technique has proven to be really effective for strain interrogation of optical fiber resonators, despite possible limitations related to its intrinsic sensitivity to environmental conditions. The above results well compare to best-reported strain sensing schemes [1-8], especially in the very-low frequency regime [34] where it approaches a tens of picostrain level. At the same time, the proposed methodology is still easy to implement as it relies on a conventional extended-cavity diode laser and almost entirely on optical methods, preventing the need for radio-frequency electronics and modulators. Admittedly, the polarization spectroscopy approach does not benefit from the excess-noise reduction of frequency-modulation techniques, such as PDH, which are supposed to achieve a shot-noise-limited performance [4]. Nevertheless, in most such cases [7, 8], the actual sensitivity is dramatically decreased by the intrinsic laser frequency jitter and the advantage of operating with a basically noise-immune method is not fully exploited, unless additional pre-stabilization devices or ultra-narrow laser sources are used.

4. Conclusion

We have demonstrated a novel interrogation technique of a FBG-resonator sensor based on a polarization-stabilized laser scheme, which extends the idea of Hansch et al. [17] and exploits the internal fiber birefringence and the additional birefringence induced by the grating-inscription process [25-28]. An *effective-medium* approach [30] enabled us to characterize the polarization spectral response of the optical system, pointing out relevant effects related to the FBG local anisotropy as a consequence of strong UV illumination. In our case, polarization spectroscopy on the cavity reflection was performed without introducing additional high-loss elements in the resonator. The derived technique proved to be capable of efficiently locking the diode-laser frequency to the cavity and detecting static and dynamic strain, within the lock bandwidth, using the intra-cavity fiber as a sensitive element. From the closed-loop correction signal, we strain-calibrated the sensor using a test perturbation signal and approached a sensitivity limit of 0.77 pε rms at 1.24 kHz, in a 1-Hz bandwidth. Moreover, our fiber-based system in the quasi-static range (2.44 Hz) achieved a sensitivity of 42 p$\varepsilon/\sqrt{\text{Hz}}$. The sensor may cover a dynamic range larger than 200 dB and is able to measure strain signals with a frequency from few Hz up to 40 kHz. The interrogation method thus proved to be comparable with that of most high-performance FBG-based sensors. A preliminary assessment of possible limitations pointed out that significant contributions in this sense come from laser frequency stability as well as intrinsic sensitivity to polarization instabilities and ambient acoustic noise. The potential in detection of dynamic strain can be further extended by use of lasers with a much narrower emission linewidth in order to fully benefit from the fiber resonator enhancement.

Acknowledgment